Slovak University of Technology in Bratislava
Faculty of Civil Engineering

Dott. Giulia Lupi

Dissertation Thesis Abstract

Mathematical and numerical methods for understanding immune cell motion during wound healing

to obtain the Academic Title of *Philosophiae Doctor (PhD.)*
in the doctorate degree study programme
9.1.9 Applied Mathematics
full-time study

Bratislava 2026

The dissertation thesis has been prepared at the Department of Mathematics and Descriptive Geometry, Faculty of Civil Engineering, Slovak University of Technology in Bratislava

Submitter:	Dott. Giulia Lupi Department of Mathematics and Descriptive Geometry Faculty of Civil Engineering, STU, Bratislava
Supervisor:	prof. RNDr. Karol Mikula, DrSc. Department of Mathematics and Descriptive Geometry Faculty of Civil Engineering, STU, Bratislava

Dissertation Thesis Abstract was sent: ....

Dissertation Thesis Defence will be held on .... at .... am/pm at the Department of Mathematics and Descriptive Geometry, Faculty of Civil Engineering, Slovak University of Technology in Bratislava, Radlinského 11, 810 05 Bratislava.

prof. Ing. Stanislav Unčík, PhD.
Dean of Faculty of Civil Engineering

Abstract

We propose a workflow to analyze macrophage motion during wound healing. These immune cells migrate toward the wound, exhibiting both directional and random motion. We smooth the trajectories to separate the two components using a curve evolution model driven by a smoothing term and an attracting term. The extracted random sub-trajectories are then analyzed via mean squared displacement to characterize the type of diffusion. The velocities along the smoothed trajectories are used as sparse samples to reconstruct the wound attractant field by solving the Laplace equation with prescribed boundary conditions. Finally, we employ the anisotropic diffusion equation for visualization; since its discretization causes oscillations and violates the min/max principle, we develop and compare different stabilized schemes. The workflow is applied to two types of wounds in zebrafish, and their similarities and differences are discussed.

Abstrakt

Navrhujeme postup na analýzu pohybu makrofágov počas hojenia rán. Tieto imunitné bunky migrujú smerom k rane a vykazujú priamy aj náhodný pohyb. Trajektórie vyhladzujeme, aby sme oddelili tieto dve zložky, pričom používame model evolúcie kriviek riadený vyhladzovaciu členom a priťahujúcim členom. Extrahované náhodné časti trajektórií sú následne analyzované pomocou strednej kvadratickej odchýlky s cieľom charakterizovať typ difúzie. Rýchlosti pozdĺž vyhladených trajektórií sú použité ako riedke vzorky na rekonštrukciu poľa atraktantu rany riešením Laplaceovej rovnice s predpísanými okrajovými podmienkami. Nakoniec využívame anizotropnú difúznu rovnicu na vizualizáciu; keďže jej diskretizácia spôsobuje oscilácie a porušuje diskrétny princíp minima/maxima, navrhujeme a porovnávame rôzne stabilizované schémy. Navrhovaný postup je aplikovaný na dva typy rán u dánia pruhovaného a sú diskutované ich podobnosti a rozdiely.

Contents

1 Introduction

Immediately after an injury, immune cells are recruited to the site of the wound. Among these, macrophages play an essential role in wound healing, as their deficiency or dysregulated behavior can lead to chronic non-healing wounds, as observed in diabetic patients. In the context of the INFLANET project, we collaborated with biologists at the University of Montpellier, who provided videos of macrophages migrating to wound sites in zebrafish, a model organism whose macrophages closely resemble those of humans. We analyzed two types of wounds differing in shape and size: a vertical wound and a circular wound. The segmentation and tracking pipeline of Park et al. [24] enabled the extraction of macrophage trajectories, revealing that macrophages exhibit both directional and random motion as they migrate toward the wound. Building on these trajectories, we developed a smoothing algorithm to separate directional motion from random motion, modeling each trajectory as a curve evolving according to a PDE comprising a curvature-driven smoothing term, an attracting term, and a tangential velocity term. We proposed two formulations of the attracting term: the Eulerian approach, based on the shortest distance from the evolving curve to the original trajectory, and the Lagrangian approach, which tracks the evolution of the lengths of the original segments. To detect the random parts, we developed two approaches: the first is based on segment disappearance during smoothing; the second identifies self-intersecting parts of the trajectories, indicating back-and-forth motion. We then studied these random parts using the mean squared displacement (MSD), finding that they consistently exhibit subdiffusive behavior, with higher diffusivity for the circular wound than for the vertical one. The velocities on the smoothed trajectories were used as sparse samples to reconstruct the wound attractant field by solving a minimization problem leading to the Laplace equation, applied independently to the two vector components and to the vector length (triple-Laplacian model). A time-dependent reconstruction was considered to analyze the temporal evolution of the field and differences across wound types. Then, we consider another minimization problem, leading to an additional smoothing step. Finally, we consider the anisotropic diffusion equation to visualize the dominant patterns of the reconstructed fields. Using the finite volume method, we developed the anisotropic diamond cell method to better account for the direction of anisotropy, improving accuracy and experimental order of convergence. To address oscillations and violations of the discrete min/max principle, we developed three stabilized schemes: S^1, S^2, and S^3 forward-backward diffusion stabilization (FBDS).

2 Biological motivation

After an injury, danger signals are released from the wound and attract immune cells to the site of the wound. The first immune cells to arrive at the site of the wound are neutrophils: they kill potential pathogens, debride the wound, and release mediators that attract other immune cells [8]. Simultaneously, monocytes begin migrating to the site of the wound and differentiate into macrophages; these cells have high plasticity, allowing them to respond to environmental signals and change their phenotype [8, 22, 9, 28, 27]. The response of these immune cells to injuries is a complex mechanism that requires a balance between the different macrophage phenotypes. Indeed, if the inflammatory response of pro-inflammatory macrophages is dysregulated, it can cause chronic inflammatory and immune diseases. For example, chronic wounds such as diabetic foot ulcers have an increased and prolonged inflammatory stage [8]. To study the motion of macrophages during wound healing, the zebrafish model is widely known among biologists, and its properties make it a suitable model to study the immune response in different contexts [25, 26, 21, 23]. This study uses *in vivo* time-lapse videos of migrating macrophages in zebrafish larvae, captured under two wound conditions: vertical wound (VW) and circular wound (CW).

3 Smoothing of macrophage trajectories

The mathematical model we propose to smooth the trajectories is based on evolving open-plane curves in the Lagrangian formulation. Namely, we solve the equation

$$\frac{\partial \mathbf{x}}{\partial t} = -\delta(\mathbf{x}, t)k\mathbf{N} + \lambda(\mathbf{x}, t)[(\mathbf{x}_0 - \mathbf{x}) \cdot \mathbf{N}]\mathbf{N} + \alpha\mathbf{T}, \tag{1}$$

where $\mathbf{x}$ is a point on the evolving curve, $-k\mathbf{N}$ is the *smoothing term* that regularizes the curve, $[(\mathbf{x}_0 - \mathbf{x}) \cdot \mathbf{N}]\mathbf{N}$ is the *attracting term* that keeps the evolving curve close to the original one, and $\delta(\mathbf{x}, t)$ and $\lambda(\mathbf{x}, t)$ are adaptively chosen positive parameters. The *tangential velocity* $\alpha\mathbf{T}$ redistributes the points on the evolving curve, guaranteeing the stability of the numerical computations.

We introduce two approaches to define the attracting term: Eulerian and Lagrangian. The first, described in [16], computes the shortest distance between a point and a curve. We call it Eulerian because we forget where the original points are located on the evolving curve, and we compute just the distance between the two curves. In the Lagrangian approach, we follow the evolution of the original points instead. This cannot be done directly because the points can also move in the tangential direction since we added the tangential velocity. It can result in a point being attracted to a point on the original curve in a completely different position, and the shape of the original curve is not preserved at all. To solve this issue, we calculate the new lengths of the original segments as if there was no tangential velocity. Hence, we can know where the original endpoints of the segments would have been on the evolving curve if there had been no tangential velocity. From this information, we define the attracting term as the vector that connects the points on the original and evolved curves belonging to the same segment. We also use the new lengths of the original segments to define the velocities on the smoothed trajectories.

We consider and compare two distinct stopping criteria. The first, described in [16], is based on the Hausdorff distance between consecutive iterations, stopping once the curve has converged to a steady state. The second, described in [17], considers the curve self-intersections and stops the iterations when the curve is unknotted. To detect such self-intersections, we use the self-intersection detection algorithm developed in [17], which is based on the method proposed in [1]. Fig. 1 shows the process for a curve; the black boxes indicate the self-intersecting parts. The main idea of self-intersection detection is to construct a background grid and check which points of the trajectory belong to the same pixel. If the points are not consecutive, then they are considered to be points where the curve is self-intersecting. This algorithm is also used to choose the parameters $\delta(\mathbf{x}, t)$ and $\lambda(\mathbf{x}, t)$

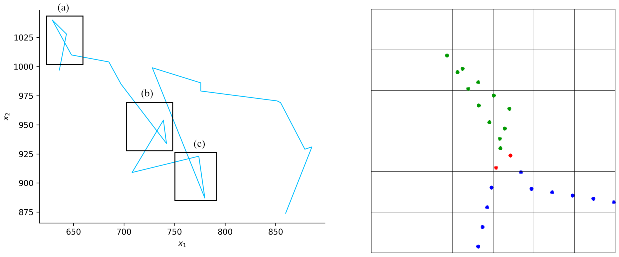

Figure 1: Top: original trajectory (light blue curve) and regions of self-intersections (black rectangles). Bottom: zoom of the top left rectangle. Grid points of the trajectory (blue asterisks), grid points where the self-intersection is detected (red asterisks), and grid points belonging to a self-intersecting part (green asterisks).

adaptively.

For the numerical discretization, we use the flowing finite-volume method [20]; the time discretization is semi-implicit, i.e., it is implicit in the intrinsic diffusion term and uses the inflow-implicit/outflow-explicit strategy for the intrinsic advection term [19]. Fig. 2 shows the result for one macrophage trajectory. The light blue curve is the original trajectory, while the green one is the smoothed curve. The adaptive choice of parameters allows us to keep the curve close to the original trajectory. We observe that in the smoothed trajectory, the curve is unknotted, resulting in a decreased length of the segments corresponding to the random

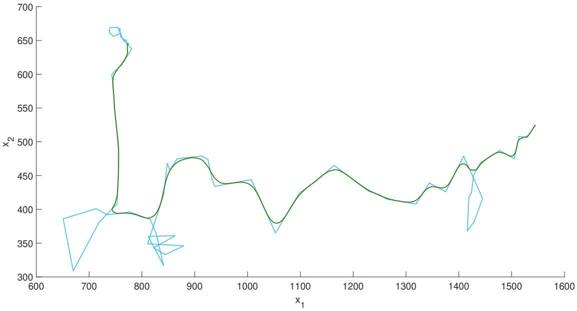

Figure 2: Original trajectory (light blue line) and results of smoothing for adaptive choice of parameters (green line). When no further self-intersections are detected, the algorithm performs 50 additional curve evolution steps before stopping.

parts of motion. Therefore, in those regions, the velocity is significantly reduced. On the other hand, in the directional parts of motion, the velocity remains close to the original one. This result is consistent with our initial assumption. Indeed, we assumed that macrophage motion is driven by the chemoattractant field, with random motion occurring in regions where the velocity field is weak. Therefore, the fact that in those regions the velocity is significantly reduced is in agreement with this hypothesis.

4 Analysis of random parts of the trajectories

To detect the random parts, we developed two methods; the first follows the evolution of the lengths of the original segments. In this approach, if a segment disappears during smoothing, we consider it to belong to a random part of the motion. A random sub-trajectory is obtained when more consecutive segments disappear. The second approach to finding the random parts considers the curve self-intersections. Indeed, the random segments are in areas of high curvature, where the cell performs a back-and-forth motion, causing the random segments to intersect. We define random segments the segments belonging to a self-intersecting part of the trajectory. Fig. 3 shows the result for the trajectories shown in Fig. 2 for the self-intersections approach: the light blue line is the original trajectory, and the red parts are the extracted random parts.

To characterize anomalous diffusion, one usually defines the *Hurst exponent* H

$$\rho(t) \sim t^{2H} \tag{2}$$

to see how the MSD grows with time. Considering the logarithm

$$\log \rho(t) \sim 2H \log t, \tag{3}$$

The dependence on time of the MSD in a log-log scale results in

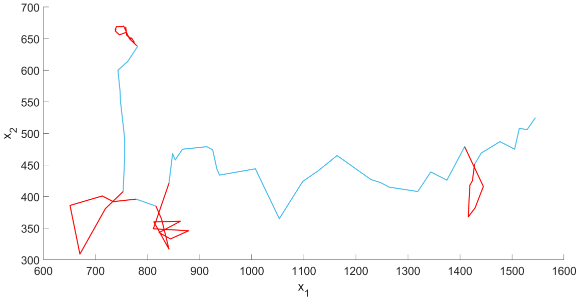

Figure 3: Extraction of random parts by curve self-intersections: original trajectory (light blue line), and extracted random parts (red lines) from curve self-intersections.

$\alpha = 2H$ being the slope of the line obtained in the double-log scaling. Fig. 4 shows the plot of MSD versus time on a log-log scale. Normal diffusion (red line) corresponds to slope $\alpha = 1$, and ballistic motion (green line) corresponds to slope $\alpha = 2$. $\alpha > 2$ gives the superballistic regime, while $1 < \alpha < 2$ gives superdiffusion. Subdiffusion is obtained for $0 < \alpha < 1$.

We consider the *time-averaged* MSD (TAMSD) [10]. Consider the i-th trajectory with initial time t_i^0 and final time T_i. Consider the data acquisition time interval ΔT: for the i-th trajectory, we have the cell position at times $(n\Delta T) + t_i^0$ for $n = 0, 1, 2.., \frac{T_i - t_i^0}{\Delta T}$, where n is the time lag. Let us denote by $K_i = \frac{T_i - t_i^0}{\Delta T}$ the final

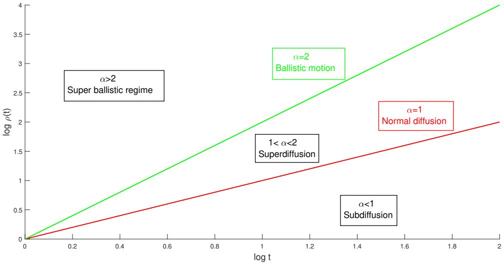

Figure 4: Plot of MSD versus time in log-log scale.

Dataset	α for disappearing segments approach	α for self-intersections approach
VW1	0.31943	0.32079
VW2	0.46355	0.50967
VW3	0.44615	0.60788

Table 1: Slope α of the line in the log-log scale for 3 vertical wound datasets.

time lag for the $i-$th trajectory. The TAMSD is defined as

$$\bar{\rho}_i(n\Delta T) = \frac{1}{K_i - n + 1} \sum_{j=0}^{K_i - n} \|\mathbf{x}_i((j+n)\Delta T) - \mathbf{x}_i(j\Delta T)\|^2. \quad (4)$$

We then considered the *ensemble average of the time-averaged* MSD (EATAMSD). Table 1 illustrates the results of the slopes α for the 2 different approaches. As can be seen, the values for the

Wound type	Dataset	α
Circular wound	CW1	0.65865
	CW2	0.80972

Table 2: Estimated α from EATAMSD for circular wound datasets

different approaches are similar, with the maximum difference in slope values between the two approaches being 0.16173 for the last dataset. Table 2 shows the results for the circular wound datasets; we used the self-intersection approach to detect the random parts. The value of α is higher in the circular wound datasets compared to the vertical wound datasets. This might be related to the more localized nature of circular wounds, which recruit nearby macrophages less exposed to competing signals, while more severe injuries attract macrophages from larger distances, reducing both their directionality and diffusive behavior.

5 Velocity vector field reconstruction

We define the model domain Ω_s by taking into account the fish boundary and the fish notochord, a region into which macrophages cannot enter (see Fig. 5). The domain Ω_r is then obtained from Ω_s by removing the squares where the sparse samples are defined – namely, the velocities evaluated along the smoothed trajectories – in such a way that Ω_r is a Lipschitz domain. We then consider the following minimization problem for the two vector components and the vector length:

$$\min_u \frac{1}{2}\left(\int_\Omega \|\nabla u\|^2 + \lambda \int_\Omega (u^0 - u)^2\right). \tag{5}$$

For the reconstruction, we consider the domain $\Omega = \Omega_r$ with parameter $\lambda = 0$. For the additional smoothing model, we instead consider $\Omega = \Omega_s$ with $\lambda > 0$. Here, u^0 is a function defined on Ω_s, see Fig. 5. Solving (5) leads to

$$-\Delta u = \lambda(u^0 - u), \tag{6}$$

with appropriate boundary conditions. The mathematical model we propose to reconstruct the 2D vector field is based on interpolating and extrapolating the given information about the vector field. For this reason, the values provided by sparse samples serve as Dirichlet conditions inside the domain. We impose zero Neumann boundary conditions on the outer boundary since we do not wish to introduce any additional information. If only the double-Laplacian [6] is used for the two vector components, the direction of the vectors changes smoothly between one another where the vectors influence each other, and is extrapolated from the Dirichlet conditions where they do not. However, it is well known that the Laplace equation averages neighboring values. Therefore, as already observed in [6], the double-Laplacian yields the desired behavior for the vector directions, but tends to shorten the vector lengths. Since our approach is based on extracting the vector field from the given information, it is natural to require that the vector lengths also are reconstructed from the prescribed Dirichlet conditions. For this reason, we apply the same minimization problem (5) to the vector lengths as well. The resulting model for vector field reconstruction, which we refer to as the *triple-Laplacian* model, consists of solving the Laplace equation three times with suitable Dirichlet and Neumann boundary conditions. In the additional smoothing model, we consider $\Omega = \Omega_s$ and impose only zero Neumann boundary conditions on the boundary, so that the values at the sparse sample locations are also smoothed. The function u^0 represents the reconstructed vector field, so that the term $\lambda(u^0 - u)$ penalizes deviations of the smoothed solution from the original reconstructed vector field, with the strength of the penalization controlled by the parameter λ. We consider both stationary and time-dependent vector field reconstruction. The model is the same in both cases; however, for the time-dependent setting, the sparse samples are prescribed only within a given time interval. Additionally, in [15], we proved the existence and uniqueness of a weak solution for both the vector field reconstruction model and the additional smoothing model. We then apply the proposed model to reconstruct the velocity vector field driving macrophages toward the wound during wound healing. To this end, we smooth the trajectories using the model described in Section 3 and use the velocity vectors defined on the smoothed trajectories to define the sparse samples for the vector field reconstruction.

We reconstruct the time-dependent velocity vector field using a 1-hour time interval. The results for CW1 are shown in Fig. 5 for the 1st, 4th, and 6th hours. The black circle indicates the region selected for the zoom shown on the right, while the purple circle marks the wound site. During the first hour, macrophages exhibit fast, directed motion toward the wound site. In the 4th hour, fast motion away from the wound is observed. Finally, in the 6th hour, the motion becomes directed again toward the wound, but it is slower and less directional than in the first hour.

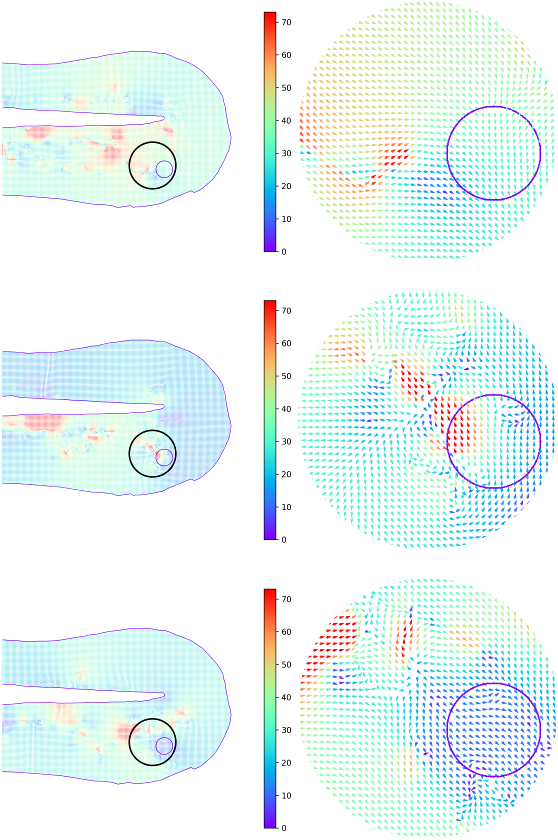

Figure 5: Reconstructed vector fields from CW1 at three time points. The black circle in the left panels indicates the region selected for the zoom shown on the right. The purple circle marks the wound site. Top: 1st hour. Middle: 4th hour. Bottom: 6th hour.

6 Anisotropic diffusion

We consider the anisotropic diffusion equation

$$u_t - \nabla \cdot (D \nabla u) = 0 \quad \text{in } \Omega, \tag{7}$$

where the diffusion tensor $D = \begin{pmatrix} \alpha & \gamma \\ \gamma & \beta \end{pmatrix}$ is symmetric positive definite, with $\alpha > 0$, $\beta > 0$. We discretize the equation using the finite volume method, where the main challenge lies in approximating the gradient on the edges of the finite volumes. The classical *Diamond Cell Method* (DCM) [4, 5] approximates the values at the vertices of the finite volumes as the average of the four neighboring cells, yielding a 9-point stencil. For the anisotropic case, a weighted average is more natural; therefore, we introduce the *Anisotropic Diamond Cell Method* (ADCM). The weights depend on the eigenvectors and eigenvalues of D, assigning larger contributions to finite volumes aligned with the dominant diffusion direction. Two variants are proposed: in the *continuous weights* (CW) version, the weights combine eigenvalue information with a linear interpolation between neighboring volumes, while in the *discontinuous weights* (DW) version, u is assumed constant within each finite volume and the weights depend solely on the eigenvalues of D.

The discretization may produce spurious oscillations, violating the *min-max principle*, which ensures that the numerical solution exhibits no overshoots or undershoots beyond the boundary data. To enforce it, we consider three stabilized schemes of Forward Backward Diffusion (FBD) type, denoted S^1, S^2, S^3, in which the coefficients are split by sign to yield an M-matrix [18, 19]. In S^1 FBDS, inspired by [19, 7, 11, 14], the right-hand side is stabilized to satisfy the min-max principle while the matrix is left unchanged, so the solution inherits the property; the drawback is a tendency to over-smooth fine details. The S^2 scheme [19] mitigates this by applying stabilization only to those finite volumes that violate the min-max principle after solving the split system; since satisfaction of the principle is not guaranteed, an iterative version is used, which converges to S^1 if needed, though in practice a single iteration suffices. The S^3 scheme is based on the *algebraic flux correction* (AFC) framework [12, 13], a generalization of flux-corrected transport (FCT) [3, 29]. The discretization matrix is transformed into a low-order M-matrix via an antidiffusive fluxes correction; the corrected fluxes $\bar{f}$ are then reintroduced so that the updated solution $u^{n+1} = \tilde{u} + \bar{f}$ satisfies $\tilde{u}^{\min} \leq u^{n+1} \leq \tilde{u}^{\max}$, where $\tilde{u}$ is the low-order solution. To mitigate the well-known *peak clipping* effect of FCT, we use the solution at the previous time step u^n as reference for the flux bounds rather than $\tilde{u}$. Fig. 6 shows a cross-section of the anisotropic Gaussian solution evolved from $t = 0.2$ to $t = 0.3$ on a grid of size $N \times N$ with $N = 160$, using a diffusion ma-

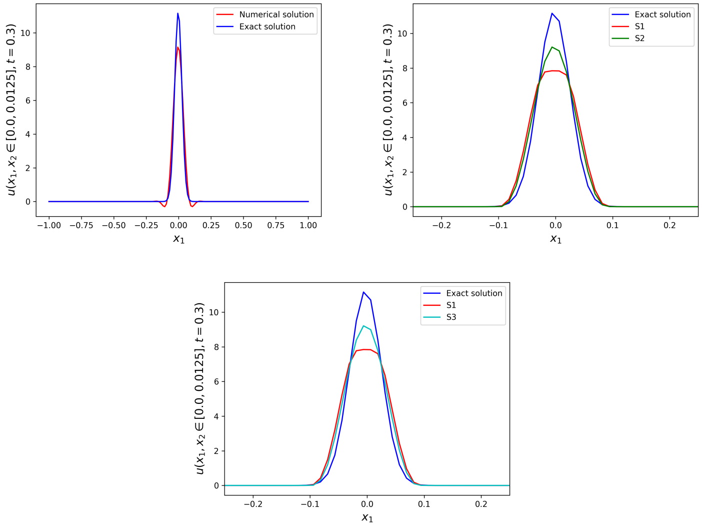

Figure 6: Cross-sections: exact solution (blue). Top left: ADCM with discontinous weights (red). Top right: S^1 stabilized solution (red), and S^2 stabilized solution (green). Bottom: S^3 stabilized solution (light blue).

trix D forming an angle $\theta = 22.5$ with the grid coordinate axes, and compares the 3 stabilization techniques for the ADCM with discontinuous weights.

The anisotropic diffusion equation can also be used to visualize vector fields [2]. By defining a spatially varying tensor D_p from the vector associated with each finite volume p, the equation diffuses preferentially along the vector direction and suppresses

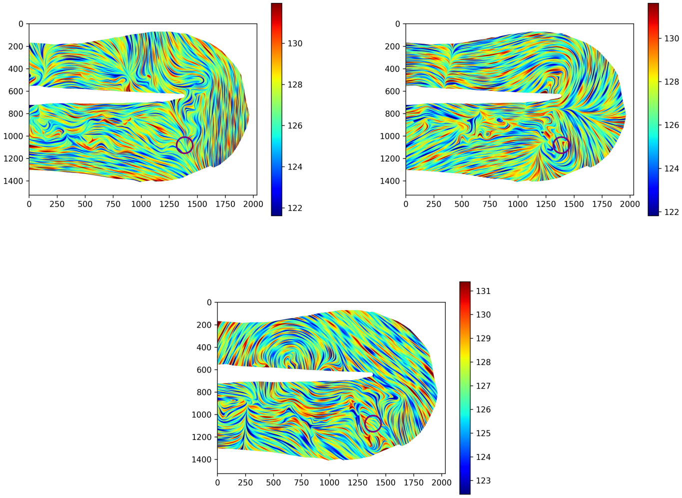

Figure 7: Non-stationary anisotropic diffusion equation applied to the reconstructed vector fields shown in Fig. 5. The purple circle indicates the wound region. Top left: 1st hour. Top right: 4th hour. Bottom: 6th hour.

diffusion orthogonally. Applied to an initial random image, the pixel values gradually align with the local vector directions, revealing the dominant structure of the field. We apply this approach to the reconstructed vector fields shown in Fig. 5; the results are visualized in Fig. 7 after 100 time steps. The circular wound region is highlighted by a purple circle in each panel.

7 Conclusion

The workflow we developed for the analysis of macrophage trajectories during wound healing in zebrafish builds upon macrophage trajectories extracted from fluorescence microscopy videos of zebrafish. We first developed a smoothing algorithm based on the evolution of curves in the Lagrangian formulation; this allowed us to separate the directional components of motion from the random ones and to compute velocities on the smoothed trajectories. We proposed two approaches to detect the random parts of the trajectories and analyzed them using the mean squared displacement. The smoothed velocities were then used as sparse samples to reconstruct the wound attractant field driving macrophages toward the injury site. We proposed a minimization problem solved independently for the vector components and the vector length, leading to the Laplace equation with prescribed boundary conditions. Then, we analyzed the temporal evolution of the wound attractant field across the two wound types. Finally, we employed the anisotropic diffusion equation to visualize the patterns of the reconstructed vector fields. For the numerical discretization via the finite volume method, we proposed the Anisotropic Diamond Cell Method, which explicitly accounts for the direction of anisotropy. To address the instabilities and violations of the discrete min/max principle, we developed and analyzed three stabilized schemes. Future research directions include the extension of the overall workflow to 3D+time datasets, the study of the reconstructed wound attractant field under different experimental conditions, and the use of the nonlinear anisotropic diffusion equation to apply iterative smoothing to the reconstructed vector field.

References

[1] M. Ambroz, M. Balažovjech, M. Medl'a, and K. Mikula, *Numerical modeling of wildland surface fire propagation by evolving surface curves*, Advances in Computational Mathematics, 45 (2019), pp. 1067–1103.

[2] J. Becker, T. Preusser, and M. Rumpf, *Pde methods in flow simulation post processing*, Computing and Visualization in Science, 3 (2000), pp. 159–167.

[3] P. Boris, Jay and L. Book, David, *Flux-corrected transport. i. shasta, a fluid transport algorithm that works*, Journal of Computational Physics, 11 (1973), pp. 38–69.

[4] W. J. Coirier, *An Adaptively-Refined, Cartesian, Cell-Based Scheme for the Euler and Navier-Stokes Equations*, PhD thesis, Michigan University, 1994.

[5] Y. Coudière, J.-P. Vila, and P. Villedieu, *Convergence rate of a finite volume scheme for a two dimensional convection-diffusion problem*, ESAIM: Mathematical Modelling and Numerical Analysis, 33 (1999), pp. 493–516.

[6] M. Fisher, P. Schröder, M. Desbrun, and H. Hoppe, *Design of tangent vector fields*, ACM Transactions on Graphics (TOG), 26 (2007).

[7] A. Handlovičová, P. Kútik, and K. Mikula, *Stabilized semi-implicit finite volume scheme for parabolic tensor diffusion equations*, Proceedings of the Conference Algoritmy, (2015), pp. 438–447.

[8] M. Hesketh, K. B. Sahin, Z. E. West, and R. Z. Murray, *Macrophage phenotypes regulate scar formation and chronic wound healing*, International Journal of Molecular Sciences, 18 (2017), p. 1545.

[9] T. J. Koh and L. A. DiPietro, *Inflammation and wound healing: the role of the macrophage*, Expert Reviews in Molecular Medicine, 13 (2011), p. e23.

[10] P. Kubala, M. Cieśla, and B. Dybiec, *Diffusion in crowded environments: Trapped by the drift*, Physical Review E, 104 (2021).

[11] P. Kutik, *Numerical solution of partial differential equations in financial mathematics*, PhD thesis, Slovak University of Technology in Bratislava, 2013.

[12] D. Kuzmin, R. Löhner, and S. Turek, *Flux-Corrected Transport, first edition*, Springer-Verlag, 2005.

[13] ——, *Flux-Corrected Transport, second edition*, Springer Nature, 2012.

[14] P. Kútik and K. Mikula, *Diamond–cell finite volume scheme for the heston model*, Discrete and Continuous Dynamical Systems - S, 8 (2015), pp. 913–931.

[15] G. Lupi and K. Mikula, *Vector field reconstruction from sparse samples by triple-laplacian*, in Proceedings of the Conference Algoritmy, 2024, pp. 85–98.

[16] G. Lupi, K. Mikula, and S. A. Park, *Macrophages trajectories smoothing by evolving curves*, Tatra Mountains Mathematical Publications, 86 (2023).

[17] G. Lupi, S. A. Park, M. Ambroz, R. Ozbilgic, M. N. Chi, G. Lutfalla, and K. Mikula, *Mathematical and numerical methods for understanding immune cell motion during wound healing*, Mathematical Modelling of Natural Phenomena, 20 (2025), p. 38.

[18] K. Mikula and M. Ohlberger, *A new level set method for motion in normal direction based on a semi-implicit forward-backward diffusion approach*, SIAM Journal on Scientific Computing, 32 (2010), pp. 1527–1544.

[19] K. Mikula, M. Ohlberger, and J. Urbán, *Inflow-implicit/outflow-explicit finite volume methods for solving advection equations*, Applied Numerical Mathematics, 85 (2014), pp. 16–37.

[20] K. Mikula, D. Ševčovič, and M. Balazovjech, *A simple, fast and stabilized flowing finite volume method for solving general curve evolution equations*, Communications in Computational Physics, 7 (2010), pp. 195–211.

[21] V. Miskolci, J. Squirrell, J. Rindy, et al., *Distinct inflammatory and wound healing responses to complex caudal fin injuries of larval zebrafish*, eLife, 8 (2019), p. e45976.

[22] D. M. Mosser and J. P. Edwards, *Exploring the full spectrum of macrophage activation*, Nature Reviews Immunology, 8 (2008), pp. 958–969.

[23] M. Nguyen-Chi, B. Laplace-Builhe, J. Travnickova, et al., *Identification of polarized macrophage subsets in zebrafish*, eLife, 4 (2015), p. e07288.

[24] S. A. Park, T. Sipka, Z. Krivá, M. Nguyen-Chi, G. Lutfalla, and K. Mikula, *Segmentation-based tracking of macrophages in 2d+time microscopy movies inside a living animal*, Computers in Biology and Medicine, 153 (2022).

[25] T. Sipka, S. A. Park, R. Ozbilgic, L. Balas, T. Durand, K. Mikula, G. Lutfalla, and M. Nguyen-Chi, *Macrophages undergo a behavioural switch during wound*

healing in zebrafish, Free Radical Biology and Medicine, 192 (2022), pp. 200–212.

[26] T. Sipka, R. Peroceschi, M. Gross, F. Ellett, C. Pescia, C. Gonzalez, G. Lutfalla, and M. Nguyen-Chi, *Damage-induced calcium signaling and reactive oxygen species mediate macrophage activation in zebrafish*, Frontiers in Immunology, 12 (2021).

[27] Z. Strizova, I. Benesova, R. Bartolini, R. Novysedlak, E. Cecrdlova, L. K. Foley, and I. Striz, *M1/m2 macrophages and their overlaps – myth or reality?*, Clinical Science, 137 (2023), pp. 1067–1093.

[28] T. A. Wynn, A. Chawla, and J. W. Pollard, *Macrophage biology in development, homeostasis and disease*, Nature, 496 (2013), pp. 445–455.

[29] T. Zalesak, Steven, *Fully multidimensional flux-corrected transport algorithms for fluids*, Journal of Computational Physics, 31 (1979), pp. 335–362.